Analysis, Design, and Implementation of a Spatially Nested Magnetic Integration Method for Inductive Power Transfer Systems

Zhuhaobo Zhang, *Student Member, IEEE*, Shaoting Zheng, Zirui Yao, *Student Member, IEEE*, Dehong Xu, *Fellow, IEEE*, Philip T. Krein, *Fellow, IEEE*, and Hao Ma, *Senior Member, IEEE*

***Abstract*—Inductive power transfer (IPT) technology uses large resonant inductors as compensation components. In this article, a spatially nested magnetic integration method is proposed to integrate discrete inductors into an IPT transformer structure. Unipolar transformer coils are employed and are decoupled orthogonally from a nested solenoidal inductance coil for various misalignment cases. The variations of the coupling coefficients and the magnetic flux density distribution are presented with the three-dimensional finite-element modeling tool. An *LCC* series compensation circuit is selected to implement the proposed method with an optimal efficiency design. A 4-kW prototype with a 160 mm airgap is implemented to demonstrate the validity of the proposed method. The experimental results show that the compact structure retains the outstanding performance and avoids significant cross coupling for lateral, vertical, and axial misalignment. The maximum conversion efficiency of the proposed system is 96.7% at full output power and stays above 91.6% throughout the misalignment range.**

***Index Terms*—Inductive power transfer (IPT), magnetic integration, misalignment tolerance, orthogonal decoupling.**

I. Introduction

COMPARED with the conventional plug-in power transfer, inductive power transfer (IPT) technology provides a convenient, weatherproof, and flexible charging option [1]–[3]. These advantages make it suitable for electric vehicle (EV) charging applications.

Manuscript received August 10, 2020; revised November 6, 2020; accepted December 10, 2020. Date of publication December 17, 2020; date of current version March 5, 2021. This work was supported in part by the National Natural Science Foundation of China under Grant 51577171 and in part by the Zhejiang University/University of Illinois at Urbana-Champaign Institute. Recommended for publication by Associate Editor M. Ponce-Silva. *(Corresponding author: Hao Ma.)*

Zhuhaobo Zhang, Zirui Yao, and Hao Ma are with the College of Electrical Engineering, Zhejiang University, Hangzhou 310058, China, and also with the Zhejiang University/University of Illinois at Urbana-Champaign Institute, Haining 314400, China (e-mail: zzhbpain@163.com; 11810009@zju.edu.cn; mahao@zju.edu.cn).

Shaoting Zheng and Dehong Xu are with the College of Electrical Engineering, Zhejiang University, Hangzhou 310058, China (e-mail: 3150103536@zju.edu.cn; xdh@zju.edu.cn).

Philip T. Krein is with the Zhejiang University/University of Illinois at Urbana-Champaign Institute, Haining 314400, China, and also with the University of Illinois at Urbana-Champaign, Champaign, IL, 61820 USA (e-mail: krein@illinois.edu).

Color versions of one or more of the figures in this article are available online at https://doi.org/10.1109/TPEL.2020.3045453.

Digital Object Identifier 10.1109/TPEL.2020.3045453

This article builds on prior work with the magnetic integration of IPT systems [14]–[19]. A spatially nested magnetic integration method is proposed to integrate discrete inductors into IPT transformers. The proposed configuration provides the advantages of compact structure, high efficiency, balanced core magnetic flux density, precise inductance adjustment, low magnetic field leakage, and low cross coupling.

In a typical IPT system for EV charging, loosely coupled transformers with large airgaps are employed. This results in a significant leakage inductance and a low coupling coefficient. To compensate, various impedance circuits have been proposed to increase power transfer capability, minimize the VA ratings of power devices, and optimize the output characteristics [4]–[13]. Four basic compensation configurations mix series and parallel connections of resonant capacitances, denoted as *S–S*, *S–P*, *P–S*, and *P–P* circuits. Their characteristics have been analyzed for various cases [4]–[6]. High-order compensation schemes, such as *LCL* and *LCC* structures, have been proposed and employed in [7]–[9] to obtain distinct features. In these cases, inductors are included in resonant tanks. Hybrid circuit methods have been explored to achieve high misalignment tolerances [10], [11] and for lithium battery charging applications [12], [13].

For compensation circuits comprising resonant inductances, past designs generally use discrete components. Considering the operating frequency in IPT systems, the inductors with ferrite cores in PQ or EE geometries are common choices. There are at least two drawbacks. First, the magnetic cores are large and the system is bulky. The volume is proportional to the inductance value and system power rating. Compared with an *LCL* compensation circuit, one of the main improvements of an *LCC* circuit is to reduce the required inductance value [8], [9]. The volume can decrease. Second, large areas of ferrite cores are employed in the conventional IPT transformers. The overall magnetic flux density is relatively low due to the large airgap between the transmitter and receiver pads. The magnetic flux density in the cores is high and close to saturation limits. This unbalance results in the magnetic core redundancy and mismatch of core losses.

The idea of integrating the compensation inductance coil into the IPT transformer was proposed in [14] to overcome discrete inductor limitations. *LCC–LCC* compensation circuits were employed. Magnetic integration on both primary and secondary sides resulted in five extra coupling coefficients, including

single-side coupling on the primary side, single-side coupling on the secondary side, and cross coupling between primary and secondary. Single-side coupling effects were studied in [14] and a detailed analysis of all coupling coefficients was presented in [15]. From the article presented in [14] and [15], the single-side coupling can be compensated by redesigning resonant capacitor values. Cross coupling decreases the system power capacity and input power factor. This complicates the system design. In [16] and [17], integrated inductance coils were designed comparable with transformer coils. They were employed as additional transmitters and receivers to transfer power. Misalignment tolerances were enhanced at the cost of high cross coupling and high reactive power. In order to reduce the cross-coupling effects, planar stacked decoupling structures were employed in [18] and [19]. Planar inductance coils were stacked on the top of planar transformer coils.

The magnetic integration methods were applied previously to the bipolar [18] and unipolar [19] transformer coil structures. The integrated inductance coils were unipolar structures in [18] and bipolar structures in [19]. Generally, unipolar structures were horizontally symmetrical and had no directional selectivity for misalignment [20], [21]. Bipolar structures had a dominant magnetic flux direction along the ferrite cores [22]. Rectangular and double D (DD) coils were employed as the unipolar and bipolar structures in [18] and [19]. When there was no misalignment, the cross-coupling coefficients were eliminated or minimized due to symmetry. This simplified the system analysis and benefited parameter design. Similar magnetic integration designs were presented in [23]–[25]. For planar stacked structures, the main drawback was that the inductance coils must be small enough. When the coils are small, cross coupling can be eliminated or minimized for various misalignment cases.

In this article, a spatially nested magnetic integration method is proposed to integrate discrete resonant inductors into an IPT transformer structure for EV charging applications. Solenoidal coils are selected as compensation inductors and are wrapped around the unipolar transformer coils and ferrite cores. Radial magnetic fluxes are generated by the transformer coils, and the tangential fluxes are generated by the inductance coils. The coils are nested spatially and the fluxes are decoupled orthogonally for various misalignment cases. This proposed configuration provides the advantages of compact structure, high efficiency, and balanced core magnetic flux density. The structure inherits the advantages of prior magnetic integration schemes [18], [19], [23]–[25] and provides at least four unique advantages, which are as follows.

1) Similar to the conventional ferrite inductors, the airgap width can be selected to provide a precise integrated inductance value.
2) The magnetic flux generated by the inductance coils is confined mostly inside ferrite cores. This decreases the magnetic field leakage.
3) The method has no physical position at which significant cross coupling occurs for various misalignment cases. This simplifies the system analysis and design.
4) The inductance coil is placed perpendicular to the transmitter coil at overlap points. The proximity effects of high-frequency ac currents are reduced.

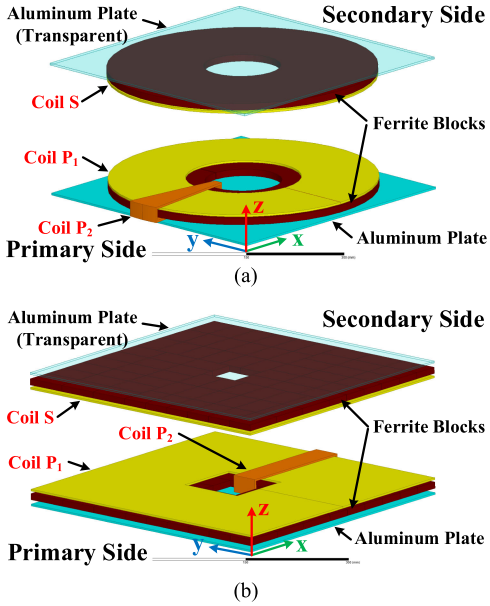

Fig. 1. Structure of the transformer with magnetic integration. (a) Circular pad structure. (b) Square pad structure.

The rest of this article is organized as follows. The transformer structure for the proposed magnetic integration method is presented in Section II. The *LCC* series compensation circuit is analyzed in Section III. The detailed design procedures and discussion are elaborated in Section IV to obtain a highly efficient system. In Section V, the experimental results are obtained from a 4-kW prototype to validate the proposed design. Finally, the conclusion is given in Section VI.

II. Transformer Structure With Magnetic Integration

The proposed transformer structure with nested magnetic integration is shown in Fig. 1. The circular and square pad structures are shown in Fig. 1(a) and (b). Each part of the transformer is marked with different colors and labeled with various material compositions. The secondary backside aluminum plate is set to be transparent. Coil P_1 and coil S are the circular or square transformer coils for the conventional use. They are designed symmetrically about the z-axis. Coil P_2 is a solenoidal coil. It is wrapped around coil P_1 and ferrite cores and is employed as the compensation inductance in high-order resonant tanks. The primary coils are nested in space.

Ferrite cores are included in the transformer to reduce the reluctance substantially. As distinct from the conventional discrete placements of ferrite bars, the proposed magnetic integration method requires a low equivalent reluctance path for the integrated inductance coil. The low reluctance path decreases the magnetomotive force (MMF) that must be imposed on the integrated inductor. Ideally, the circular pad structure in Fig. 1(a) works well. In practice, rectangular ferrite blocks are more readily available. Consequently, the square pad structure in Fig. 1(b) is selected and the corresponding design procedures are implemented in Section III.

Circular and square coils generate a symmetrical magnetic flux. The primary flux direction associated with the solenoidal

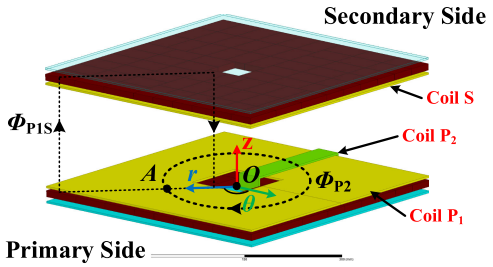

Fig. 2. Magnetic flux paths and coordinate system transformation for the square pad structure.

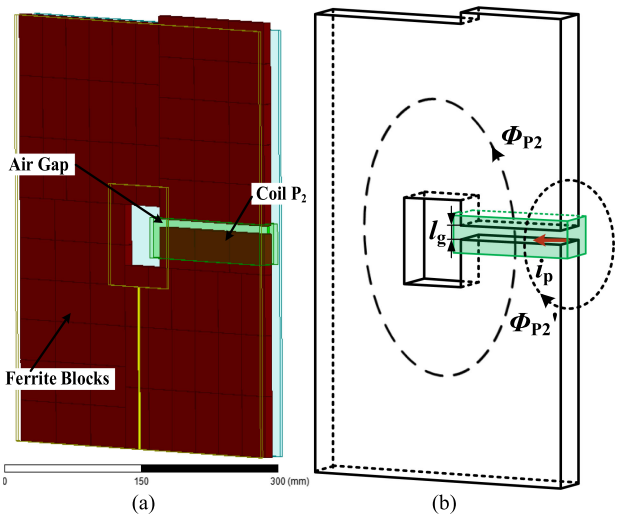

Fig. 3. (a) Side view of transformer structures for the primary side. (b) Magnetic flux paths generated by coil P_2.

coils is along the ferrite cores. As shown in Fig. 2, point A is taken as an example to illustrate the magnetic flux paths and a coordinate system transformation for the square pad structure. The original cartesian coordinate system x–y–z can be transformed into cylindrical r–θ–z coordinates. The magnetic flux generated by square coil P_1 is denoted as Φ_{P1S} and is along the radial direction. This is the main coupling flux between the primary and secondary sides. The magnetic flux generated by solenoidal coil P_2 is denoted as Φ_{P2} and is along the tangential direction. Fluxes Φ_{P1S} and Φ_{P2} intersect perpendicularly and are decoupled orthogonally. These flux characteristics hold for every point within square ferrite cores on the primary side, although the geometry is approximate near the corners. Consequently, coil P_2 is decoupled from transmitter coil P_1. A side view of the primary transformer structure is shown in Fig. 3(a). Coil P_1 is transparent in this view. The magnetic flux paths generated by coil P_2 are shown in Fig. 3(b). Φ_{P2}' represents a leakage flux path. Here, l_g represents the width of the airgap within the structure. As in the conventional ferrite inductors, flux Φ_{P2} is confined inside the core and gap. In principle, solenoidal coil P_2 can be installed on any side of the square cores but the optimal placement is on the same side as the airgap. In this case, the airgap decreases the flux linkage between coils P_2 and S. This reduces cross-coupling coefficients and benefits magnetic integration. Consequently, coil P_2 is decoupled approximately from the receiver coil S. These decoupling principles hold for various misalignment cases, including lateral, vertical, and axial ones. Coils P_1 and P_2 are placed perpendicularly at overlap points and the proximity effects of high-frequency ac currents are reduced.

As shown in Fig. 3(a), the ferrite blocks are tightly spaced to minimize extraneous airgaps with the coils arranged along the surface. The cores are designed to be symmetrical about the z-axis except for the intentional airgap inside solenoidal coil P_2. The airgap is selected in a manner consistent with the design of the conventional ferrite power inductors. A large airgap can decrease the magnetic flux density and core losses but requires more turns. The airgap width value is a compromise. Compared with the magnetic integration methods in [14]–[22], the nested structure will not increase the magnetic field leakage. Square aluminum plates behind the primary and secondary pads will help shield the backside magnetic flux. This reduces the leakage and improves the coupling performance of the transformer.

TABLE I
SPECIFICATIONS OF PROTOTYPE IPT SYSTEM

Parameters	Symbols	Values
Nominal power rating	P_o	4 kW
Input voltage	V_{in}	350 V
Output voltage	V_o	350 V
Nominal load resistance	R_L	30 Ω
Transformer length	/	420 mm
Transformer width	/	420 mm
Transformer air gap	/	160 mm
Ferrite blocks	/	60x40x10 mm

III. SYSTEM ANALYSIS AND DESIGN PROCEDURES

In this section, an *LCC* series compensation circuit is selected to implement the proposed magnetic integration method. The circuit characteristics are analyzed. The design procedures for transformer dimensions and resonant elements are presented based on the system specifications in Table I. In Table I, the system power and voltage ratings are predetermined to match an actual prototype for EV charging applications. An area of 420 mm in length and 420 mm in width is set up in the prototype and reserved for the IPT transformer. The airgap between the transformer pads is held at 160 mm in accordance with the Z2 class in standard J2954 [26]. The ferrite block dimension is 60 mm × 40 mm × 10 mm.

A. Analysis of the Implemented Circuit Topology

The circuit topology with *LCC* series compensation is shown in Fig. 4(a). A mutual inductance model is used for the loosely coupled transformer, as represented by the shaded area. The primary circuit consists of a full-bridge inverter and a transmitter coil with the *LCC* compensation. The inverter is composed of four power MOSFETs (S_1–S_4). The secondary circuit consists of a full-bridge rectifier (diodes D_1–D_4) and a receiver coil with single capacitor compensation. Inductances L_{p1}, L_{p2}, and L_s correspond to the self-inductances of coils P_1, P_2, and S. Their

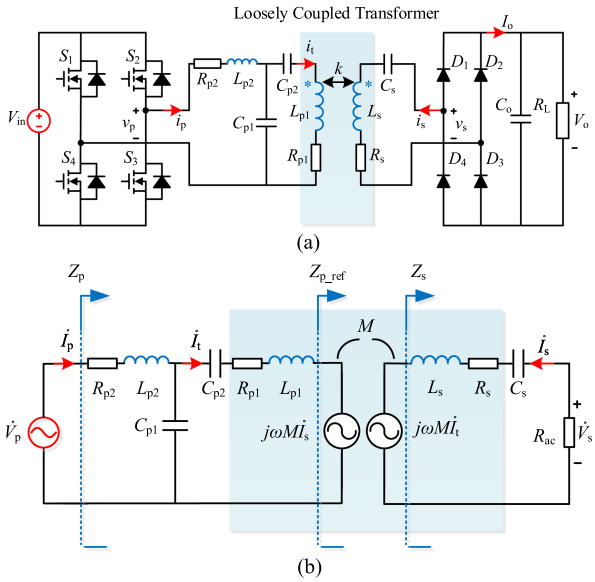

Fig. 4. (a) Circuit topology with *LCC* series compensation. (b) Equivalent mutual inductance circuit model.

parasitic resistances are represented as R_{p1}, R_{p2}, and R_s. The parameter k_{P1S} is defined as the coupling coefficient between coils P_1 and S. The other coupling coefficients are k_{P1P2} and k_{P2S}, but these are nearly zero because of decoupling and are not shown in Fig. 4.

The fundamental harmonic approximation method [27] is used to analyze the basic circuit characteristics. The equivalent mutual inductance circuit model is shown in Fig. 4(b). Ignoring the high-order harmonics, define

$$\begin{cases} V_p = \frac{4}{\pi} V_{in} \\ R_{\rm ac} = \frac{8}{\pi^2} R_L \end{cases} \tag{1}$$

where $V_{\rm in}$ and V_o are the system input and output dc voltages, respectively. Here, V_p and V_s are the magnitudes of the fundamental harmonic voltages after the inverter and before the rectifier, respectively. Z_p, $Z_{p\text{ref}}$, and Z_s are the equivalent impedance variables seen from various terminals of the circuit. R_L and $R_{\rm ac}$ are the load and system equivalent load seen after and before the diode rectifier, respectively.

Impedance characteristics can be obtained from loop equations. The corresponding resonant condition [9] is given by

$$\omega = 2\pi f_s = \frac{1}{\sqrt{L_{p2}C_{p1}}} = \frac{1}{\sqrt{L_s C_s}} = \sqrt{\frac{1}{L_{p1}}\left(\frac{1}{C_{p1}} + \frac{1}{C_{p2}}\right)} \tag{2}$$

where ω represents the system frequency in rad/s. For the resonant condition, Kirchhoff's voltage law gives

$$\begin{cases} \dot{V}_p = (R_{p2} + j\omega L_{p2})\,\dot{I}_p + \frac{1}{j\omega C_{p1}}(\dot{I}_p - \dot{I}_t) \\ 0 = j\omega M\,\dot{I}_s + (R_{p1} + j\omega L_{p1} + \frac{1}{j\omega C_{p2}})\,\dot{I}_t - \frac{1}{j\omega C_{p1}}(\dot{I}_p - \dot{I}_t) \\ 0 = \dot{I}_s\,R_{\rm ac} + j\omega M\,\dot{I}_t - \dot{I}_s(R_s + j\omega L_{s1} + \frac{1}{j\omega C_{s1}}). \end{cases} \tag{3}$$

The circuit voltage gain, output power, and system efficiency can be derived and are given by

$$\frac{V_{\rm o}}{V_{\rm in}} = \frac{\omega^2 M L_{p2} R_{ac}}{R_{p2}(\omega M)^2 + (R_{ac} + R_s)[(\omega L_{p2})^2 + R_{p1}R_{p2}]} \tag{4}$$

$$P_o = \mathrm{Re}[\dot{V}_s\,(\dot{I}_s)^*] = \frac{{V_p}^2 \omega^4 M^2 {L_{p2}}^2 R_{ac}}{\left\{R_{p2}(\omega M)^2 + (R_{ac} + R_s)[(\omega L_{p2})^2 + R_{p1}R_{p2}]\right\}^2} \tag{5}$$

$$\eta = \frac{P_{\rm out}}{P_{\rm in}} = \frac{\mathrm{Re}[\dot{V}_s\,(\dot{I}_s)^*]}{\mathrm{Re}[\dot{V}_p\,(\dot{I}_p)^*]} = \frac{\omega^4 M^2 {L_{p2}}^2 R_{ac}}{\left\{R_{p2}(\omega M)^2 + (R_{ac}+R_s)[(\omega L_{p2})^2 + R_{p1}R_c]\right\}[(\omega M)^2 + R_{p1}(R_{ac}+R_s)]}. \tag{6}$$

From (1) and (6), the optimal load matching resistance *R*opt *L* to maximize system efficiency η can be obtained by setting the derivative of η to be zero

$$\frac{d\eta}{dR_{\rm ac}} = 0. \tag{7}$$

The matching value can be found from (7) as (8), shown at bottom of next page, showing that *R*opt *L* is linked to parasitic resistances, compensation inductance L_{p2}, and mutual inductance *M* for a fixed operating frequency. Typically, the parasitic resistances are small compared with the load resistance *R L* and mutual inductance impedance ωM for EV charging applications. This allows (4) to be simplified, leading to the voltage ratio

$$\frac{V_{\rm o}}{V_{\rm in}} = \frac{\omega^2 M L_{p2} R_{ac}}{R_{p2}(\omega M)^2 + (R_{ac} + R_s)[(\omega L_{p2})^2 + R_{p1}R_c]} \approx \frac{M}{L_{p2}}. \tag{9}$$

Consequently, the circuit output with this type of compensation behaves as an approximate voltage source. This load-independent characteristic provides flexibility for the system analysis and benefits the parameter design. One drawback of the *LCC* circuit is the need for the primary-side resonant inductor. The system volume increases with the conventional ferrite cores. The proposed magnetic integration method is implemented to solve this problem.

B. Selecting Transformer Dimensions

Loosely coupled transformers are inherent in an IPT system. IPT transformer pads seek to maximize quality factor Q and coupling coefficient k, while minimizing weight and volume. Based on the proposed nested magnetic integration method, as shown in Fig. 2, the top views of the primary and secondary sides are shown in Fig. 5. The design seeks to maximize the main coupling coefficient k_{P1S}. Considering the transformer dimensions in Table I, the outlines of transformer coils, aluminum plates, and ferrite cores are designed to be square. Transformer dimensions for the ferrite and coil hole widths, as defined in Table II, have been optimized with a 3-D finite-element modeling (FEM) tool to seek the maximum coupling coefficient between the transformer coils given the 420 mm × 420 mm limits on the overall dimensions. The tool uses an ac analysis to include

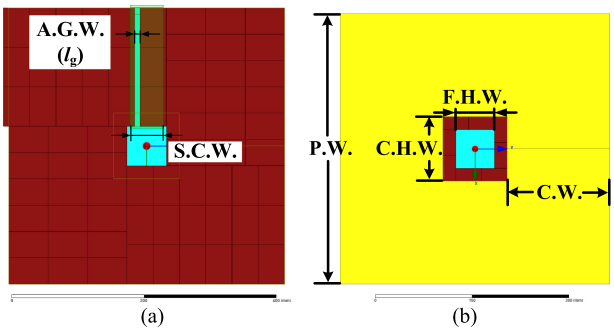

Fig. 5. Top view of transformer structures with designed parameters for (a) primary side and (b) secondary side.

TABLE II
DESIGNED PAD DIMENSIONS

Parameters	Symbols	Values (mm)
Aluminum length	**A.L.**	420
Square pad width	**P.W.**	420
Square coil width	**C.W.**	320
Ferrite hole width	**F.H.W.**	60
Coil hole width	**C.H.W.**	100
Solenoidal coil width	**S.C.W.**	40
Air gap width	**A.G.W. (l_g)**	8

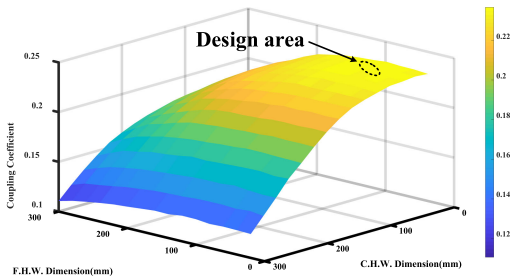

Fig. 6. Simulation results of the main coupling coefficient for various transformer structure dimensions.

eddy currents. The nominal frequency is 85 kHz. The simulation results are shown in Fig. 6. The low values of ferrite and coil hole widths result in high coupling coefficients. The maximum coupling coefficient occurs within the dotted area, as shown in Fig. 6. This should serve as the target design area. The hole widths are determined, as given in Table II, and the maximum coupling coefficient is 0.235 for a 160 mm transformer airgap. This also allows sufficient space for the inductance coil. Along with the coupling coefficient, self-inductances can be obtained from the FEM simulation results with a single-turn coil. As shown in Fig. 5(a), 72 ferrite blocks are employed on the primary side and pressed tightly to minimize extraneous airgaps. A 0.05 mm spacing is modeled among the ferrite blocks to help consider the effects of mechanical tolerances. Ferrite placements are identical on the secondary side except for the designed airgap l_g to implement the magnetic integration.

The second design step is to implement the magnetic integration. From the analysis in Section II, inductance coil P_2 is decoupled from the transmitter and receiver coils. The airgap width l_g, as shown in Fig. 5, and the turns count of coil P_2 N_{p2} are compromise choices similar to those in the conventional power inductor designs. The magnetic flux Φ_{P2} is given by

$$\Phi_3 = \int\int \vec{B_{\text{core}}} \cdot d\vec{S_{\text{core}}} \tag{10}$$

where B_{core} is the magnetic flux density generated by solenoidal coil P_2 and dS_{core} is the cross-sectional normal vector. From Faraday's and Ampere's laws, the coil self-inductance can be represented as

$$L = \frac{N_c \Delta B_{\max} A_e}{\Delta I_{p,\max}} = \frac{\mu_e {N_{p2}}^2 A_e}{l_e} \tag{11}$$

where A_e, μ_e, and l_e are the fundamental magnetic parameters and represent the effective cross-sectional area, core permeability, and effective magnetic path length for Φ_{P2}, respectively. The path length can be derived and is given by

$$l_e = l_{\text{core}} + \mu_r l_g \tag{12}$$

where μ_r represents the core relative permeability. From (11) and (12), a large airgap width decreases core magnetic flux density B but increases coil turns. The airgap width value is a compromise. From the Steinmetz formula

$$P_{\text{core}} = K_c f^{\alpha} B_{\max}^{\beta} \tag{13}$$

core losses will decrease when B is reduced for a fixed operating frequency. When the coil inductance and other circuit parameters are fixed, the coil current density is almost unchanged. A decrease in core losses can balance higher copper losses linked to more coil turns.

For loosely coupled transformers, two points are distinct from the conventional magnetic designs. First, a large airgap is easier to implement and has little influence on the main coupling characteristics. Second, due to the large volume of ferrite cores used in the IPT systems, core loss is a major issue and low flux density is important. Given the complicated geometry, the FEM simulation is useful for the inductance coil parametric selection. The simulation results, based on the ac field analysis, for the self-inductance L_{p1} and core losses, given various airgap widths, are shown in Fig. 7(a). Due to the large area of ferrite cores, narrow airgaps have little impact on the primary coil inductance L_{p1}. From Fig. 7(a), the maximum self-inductance deviation is below 2 μH. The simulation results for core losses are also shown in Fig. 7(a). The MMF imposed on the integrated inductance is adjusted, as the airgap width changes to keep the coil inductance value constant. In Fig. 7(a), core losses decrease as the airgap

$$R_L^{\text{opt}} = \frac{\pi^2}{8}\sqrt{\frac{(\omega^2 M L_{p2})^2\left[\frac{M^2 R_{p2}}{{L_{p2}}^2} + \frac{2R_s R_{p2} R_{p1}}{\omega^2 {L_{p2}}^2} + \frac{R_{p1}{R_s}^2}{\omega^2 M^2} + R_s\right] + {R_{p1}}^2 R_{p2} {R_s}^2}{\omega^2 {L_{p2}}^2 R_{p1} + {R_{p1}}^2 R_{p2}}} \tag{8}$$

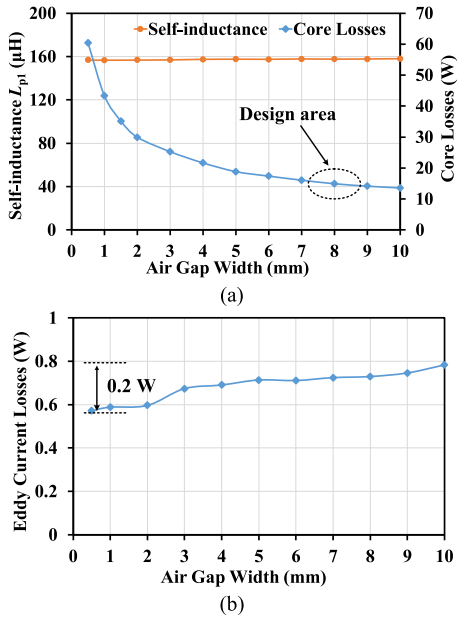

Fig. 7. Simulation results of (a) core losses and the coil self-inductance L_{p1} and (b) eddy current losses inside aluminum plates for various airgap widths.

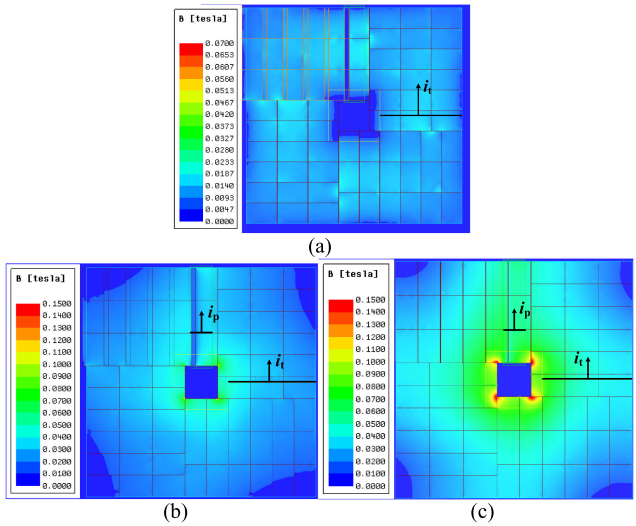

Fig. 8. Ferrite cores magnetic flux density distribution of the transformer. (a) Without magnetic integration. (b) With magnetic integration and 8 mm airgap width. (c) With magnetic integration and 1 mm airgap width.

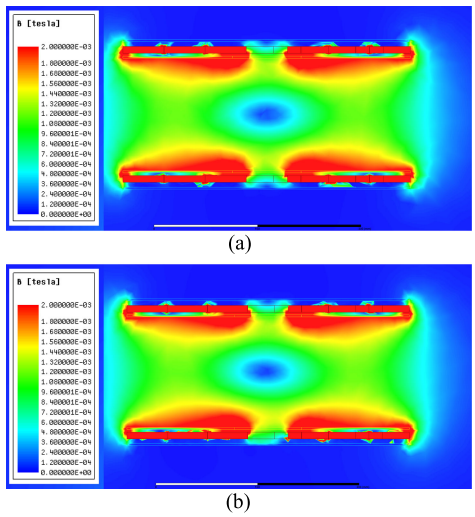

Fig. 9. Airgap magnetic flux density distribution of the transformer. (a) Without magnetic integration. (b) With magnetic integration.

width increases. The dotted area in Fig. 7(a) shows good choices for airgap width values.

The simulation results for eddy current losses inside the aluminum plates, given various airgap widths, are shown in Fig. 7(b). The losses increase as the airgap width increases, but the maximum eddy current loss is below 1 W. This is due to the following three aspects. First, ferrite cores are closely packed. This limits the leakage flux. Second, the airgap width is narrow compared with the transformer dimensions. Third, as in the conventional IPT transformers, nonmetallic materials, such as epoxy resin boards, are used between the ferrite cores and aluminum plates for support and isolation. This increases the thickness of the transformer pads and decreases the eddy current losses in the aluminum plates.

For the transformer, the magnetic flux density distribution in the ferrite cores is shown in Fig. 8(a)–(c). The grid lines in Fig. 8 outline the frames of ferrite blocks to demonstrate the flux distribution. As shown in Fig. 8(a), due to the large airgap between the primary and secondary sides, the average flux density is below 0.025 T when the primary coil MMF is set to 250 A. The average flux density increases when the integrated inductance coil is employed. As shown in Fig. 8(b), an 8 mm airgap leads to an average flux density of approximately 0.04 T when the integrated inductance MMF is set to 90 A. When the airgap width and inductance MMF are set to 1 mm and 48 A, the B distribution is as shown in Fig. 8(c) and the average flux density is approximately 0.08 T. These values were determined for the nominal power. In Fig. 8(c), the maximum flux density occurs near the inner corners of the cores. The value is approximately 0.22 T. It increases rapidly as the airgap width decreases and tends toward the saturation for higher power ratings. In practice, a desired flux density limit can be achieved by adjusting the airgap width to avoid local saturation. The system parameters, such as coil inductances and coupling coefficients, are then nearly constant over the intended current ranges. Decreased flux densities and core losses benefit the system efficiency, although they tradeoff against the power transfer capability.

The magnetic flux density distribution in the airgap between the primary and secondary sides is shown in Fig. 9. The primary and secondary coil currents operate in phase to produce the maximum flux density. The flux generated by the integrated inductance coil is confined mostly in the ferrite cores. As shown in Fig. 9, the spatial magnetic field leakage is almost unchanged for cases with and without magnetic integration. This characteristic is an advantage of the proposed method for EV charging applications.

Based on the above-mentioned procedures, the final design dimensions are listed in Table II. To demonstrate the coupling

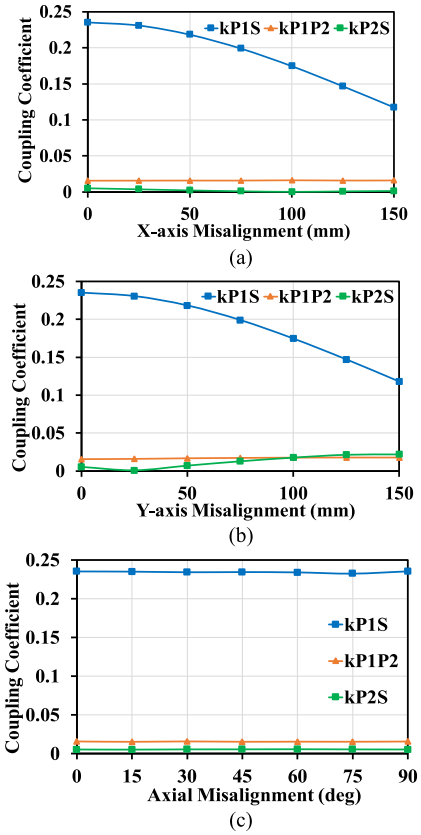

Fig. 10. Coupling coefficients for (a) lateral (*x*-axis) misalignment, (b) vertical (*y*-axis) misalignment, and (c) axial misalignment.

performance, the simulation results of coupling coefficients versus lateral, vertical, and axial misalignment are shown in Fig. 10. A 150-mm lateral or vertical misalignment is considered. The variations of coupling coefficients k_{P1S}, k_{P1P2}, and k_{P2S} are shown in Fig. 10(a) and (b) when the vertical or lateral offset is zero. Similar coefficients are shown in Fig. 10(c) with axial misalignment. In Fig. 10, coupling characteristics behave identically in the lateral and vertical directions. From the simulation results, the maximum cross-coupling coefficient is about 0.022 within the allowed misalignment range. There is no location at which a significant cross coupling is observed.

C. Selecting Resonant Element Parameters

The resonant circuit parameters can be selected based on the circuit characteristics, as discussed in Section III-A. Compensation inductance L_{p2} and mutual inductance M should be chosen as in (9). The optimal load resistance expression (8) can be simplified for the fixed voltage gain as (14), as shown at bottom of this page. Ignoring the high-order parasitic resistance terms,

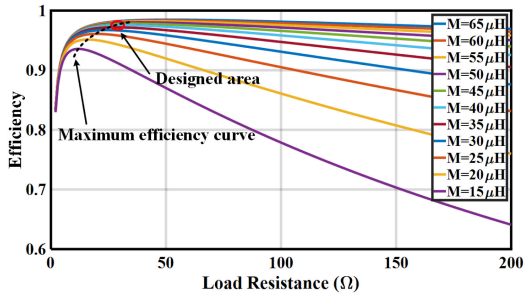

Fig. 11. Curves of the system efficiency for various load resistances and mutual inductances.

an approximate expression is

$$R_L^{\text{opt}} \approx \frac{\pi^2}{8}\omega M\sqrt{\frac{R_{p2}+R_s}{R_{p1}}}. \tag{15}$$

In (15), the optimal load resistance *R*opt *L* is proportional to the mutual inductance *M*. The curves of system efficiency for various mutual inductances and load resistances are shown in Fig. 11. Parasitic resistances R_{p1}, R_{p2}, and R_s are set to the estimated values of 0.2, 0.1, and 0.2 Ω, respectively, as a way to include losses. In accordance with standard J2954 [26], the system operating frequency is 85 kHz, although this can be adjusted slightly to match the resonance.

For the nominal 30 Ω load resistance, the optimal mutual inductance value falls within the dotted design area in Fig. 11. Higher mutual inductance brings little efficiency improvement at the expense of more coil turns. Based on the mutual inductance selection and the nominal coupling coefficient obtained from Fig. 6, the product of transmitter and receiver coil self-inductances is determined. For symmetry and to simplify the design, L_{p1} and L_s are set equal. The mutual inductance selection can be adjusted during the design with the choice of transformer turns count. The resonant capacitor parameters can be determined from (2).

D. Analysis of the Primary Parasitic Capacitances

As shown in Fig. 2, the inductance coil P_2 is wrapped around the transmitter coil P_1 and ferrite blocks on the primary side. The two-layer structure leads to parasitic capacitances between two primary windings. The parasitic capacitances of transformers have been analyzed and elaborated in [28]–[30], and an equivalent circuit can be developed, as shown in Fig. 12(a). The parasitic capacitances can be modeled by six independent capacitors. The values of these six capacitors are given by

$$C_1 = C_2 = -\frac{1}{6}C_0, \quad C_3 = C_4 = \frac{1}{3}C_0, \quad C_5 = C_6 = \frac{1}{6}C_0 \tag{16}$$

$$R_L^{\text{opt}} = \frac{\pi^2}{8}\sqrt{\frac{(\omega M)^4(R_{p2}+R_s)+(\omega M)^2(2R_sR_{p2}R_{p1}+R_{p1}R_s{}^2)+R_{p1}{}^2R_{p2}R_s{}^2}{(\omega M)^2R_{p1}+R_{p1}{}^2R_{p2}}} \tag{14}$$

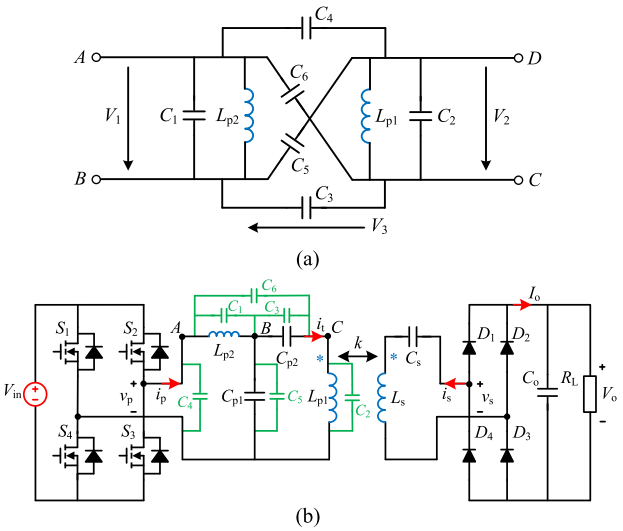

Fig. 12. (a) Equivalent circuit of two primary windings. (b) Implemented *LCC* series circuit with primary parasitic capacitances.

where C_0 represents the static winding capacitance. The coil isolation material is polyimide with relative permittivity. Using a parallel-plate capacitor model [30], C_0 can be estimated as

$$C_0 = \varepsilon_0 \varepsilon_r \frac{S}{d} \approx 8.85\times10^{-12}\times3.4\times\frac{0.007}{0.5\times10^{-3}}\text{F} = 0.42\,\text{nF}. \tag{17}$$

The parameter S represents the overlap area of the two primary windings. C_0 is relatively low because of the low solenoidal coil width, as given in Table II.

The *LCC* series circuit with primary parasitic capacitances is shown in Fig. 12(b). Capacitors C_3 and C_5 are in parallel with resonant capacitors C_{p2} and C_{p1} and do not change the circuit operation. This also applies to capacitors C_1 and C_2 because their values are negative. They behave as inductances with high values and have little impact compared with coil inductances L_{p1} and L_{p2}. Capacitors C_4 and C_6 can be analyzed using star-delta transformations. Considering these capacitors, the maximum deviation of resonant parameters from their nominal values is approximately 0.7% and is comparable with component tolerances. Consequently, parasitic capacitances have little influence on the system design procedures and will have their impact on the small adjustment of frequency to match the actual resonance.

IV. Experimental Results

A 4-kW IPT charging system prototype with *LCC* series compensation was built and tested to demonstrate the feasibility of the proposed nested magnetic integration method. A picture of the primary square coil with its integrated solenoidal inductance coil is shown in Fig. 13(a). The transformer matches the dimensions in Table I. The transmitter and receiver coil arrangements are identical for the primary and secondary sides except for the airgap within the primary-side ferrite cores. A picture of the experimental prototype is shown in Fig. 13(b). The measured parameters of resonant components are listed in

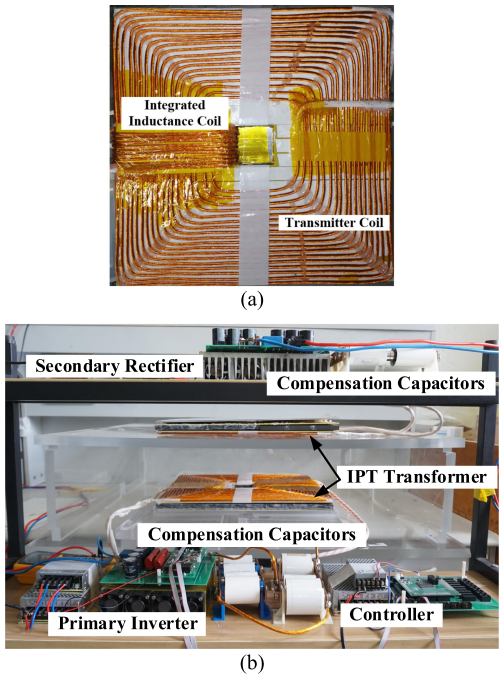

Fig. 13. (a) Primary transformer with magnetic integration. (b) 4-kW IPT experimental prototype.

TABLE III
Measured Resonant Tank Parameters

Parameters	Symbols	Values
Transmitter coil turns	N_{p1}	18
Transmitter coil inductance	L_{p1}	169.0 μH
Transmitter coil ac resistance	R_{p1}	0.223 Ω
Receiver coil turns	N_s	18
Receiver coil inductance	L_s	161.7 μH
Receiver coil ac resistance	R_s	0.222 Ω
Integrated inductance coil turns	N_{p2}	9
Integrated inductance	L_{p2}	37.62 μH
Integrated inductor ac resistance	R_{p2}	0.074 Ω
Primary resonant capacitance	C_{p1}	96.14 nF
	C_{p2}	26.61 nF
Secondary resonant capacitance	C_s	21.78 nF

Table III. The IPT system consists of an H-bridge inverter, the primary and secondary pads with their compensation capacitors, a diode rectifier bridge, and load resistances. A chroma dc source (62 100 H-450) provides the input power. An SiC MOSFET module (SK45MH120TSCp) from Semikron is used for the full-bridge inverter and SiC Schottky diodes are used for the rectifier. Polypropylene film capacitors in series and parallel combinations are used as compensation components. The controller is implemented with a Texas Instruments TMS320F28335 DSP to generate switching signals for the inverter. The operating frequency is set to 85 kHz. The system operates an open loop with 350 V input. The nominal load resistance is 30 Ω.

The experimental results for coupling coefficients given lateral, vertical, and axial misalignment are shown in Fig. 14(a)–(c). The measured coupling coefficients are slightly lower than those in the simulation results. The deviations are less than 5%. Minor differences are due to the simplifications of the

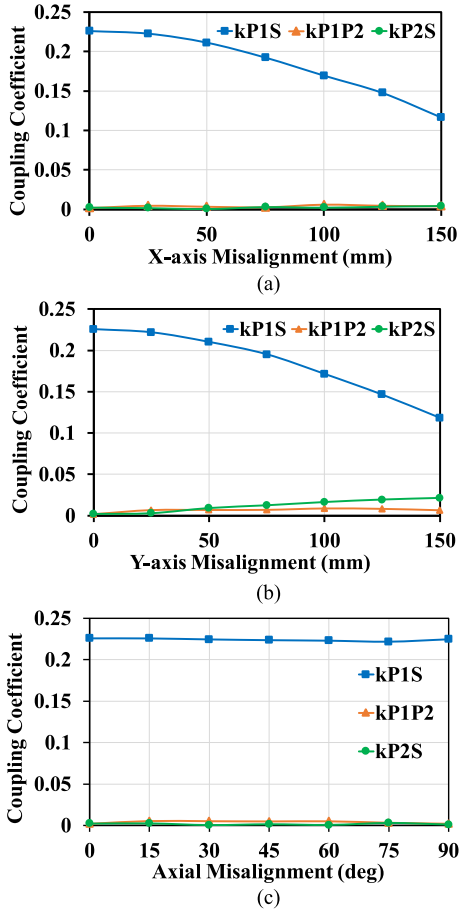

Fig. 14. Measured coupling coefficients for (a) lateral (*x*-axis) misalignment, (b) vertical (*y*-axis) misalignment, and (c) axial misalignment.

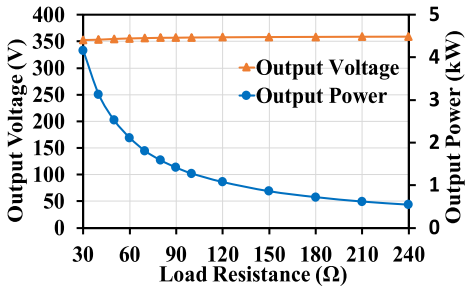

Fig. 15. System output characteristics for various load resistances.

transformer model, gaps among ferrite cores, and dimensional tolerances in the actual prototype. From the measured results, the maximum cross-coupling coefficient is about 0.02 across the allowed misalignment range. This verifies that the integrated inductance coil is approximately decoupled from the transformer coils for various misalignment cases. The system has no position at which a significant cross coupling occurs.

The experimental results for system output characteristics and dc–dc conversion efficiency given various load resistances are shown in Figs. 15 and 16. Three cases have been defined for the tests. These are listed in terms of the measured values in Table IV. Integrated inductors are employed in cases I and II with different airgap widths and inductance coil turns. The airgap widths are

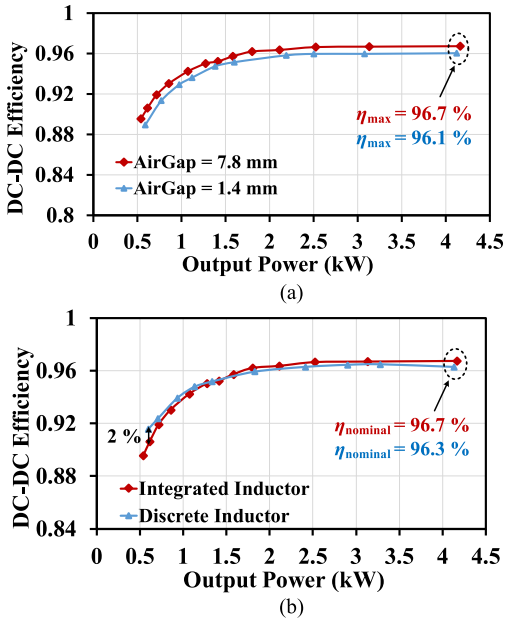

Fig. 16. DC–DC conversion efficiency for various output powers for (a) cases I and II, and (b) cases I and III.

TABLE IV
MEASURED INDUCTANCE COIL PARAMETERS FOR THREE CASES

Cases	Parameters	Symbols	Values
Case I	Integrated inductance coil turns	N_{p2}	9
	Integrated inductance	L_{p2}	37.62 μH
	Air gap width	l_g	7.8 mm
Case II	Integrated inductance coil turns	N_{p2}	5
	Integrated inductance	L_{p2}	36.86 μH
	Air gap width	l_g	1.4 mm
Case III	Discrete ferrite core geometry	/	PQ 40/40
	Discrete ferrite core material	/	PC 40
	Discrete core effective area	A_e	210 mm^2
	Discrete core effective volume	V_e	19.7 cm^3
	Discrete inductance	L_{p2}	37.77 μH
	Discrete inductance coil turns	N_{p2}	10

7.8 and 1.4 mm, respectively. An external discrete inductor is employed in case III with a pair of PQ 40/40 ferrite cores. The ferrite core material is PC 40. Other resonant parameters are identical to those in Table III. The discrete inductance value is nearly the same as that for the two integrated cases. This leads to almost identical system voltage gains and inductor currents for these three cases.

From Fig. 15, the output voltage stays close to 350 V and an operating model based on an approximate voltage-source output is appropriate. The maximum voltage deviation shows less than 3% error due to the influences of parasitic resistances. The nominal output power is close to 4 kW and the power decreases to 550 W at the 240 Ω light-load resistance condition. From Fig. 16, the tendency toward the efficiency change coincides with Fig. 12. For integrated inductor cases, when the airgap width is 7.8 mm, the maximum system efficiency is 96.7% for the nominal output power and decreases to 89.5% for 500 W output power. When the airgap width is 1.4 mm, the core losses

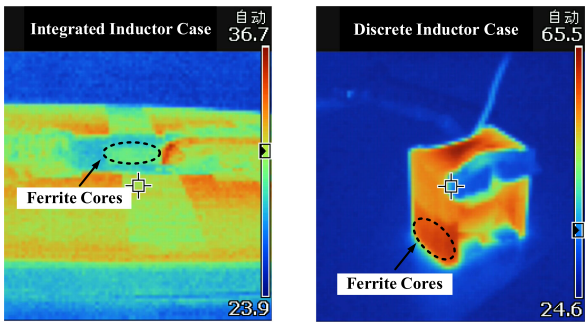

Fig. 17. Thermal camera results of the operating temperatures for nominal output power with (a) integrated inductor and (b) external discrete inductor.

increase and system efficiency is reduced. At the nominal output power, the efficiency decrease is approximately 0.6%. For the discrete inductor case, the maximum flux density in the ferrite cores is set to about 0.28 T and the maximum system efficiency is 96.3% for the nominal output power. This is slightly lower compared with case I with an integrated inductor. The system efficiency decreases to 91.6% at 600 W output power. This is 2% higher than for case I. The efficiency increase is due to the reduced inductor copper loss at light load.

The thermal camera results of operating temperatures at nominal output power with an integrated inductor and with an external discrete inductor are shown in Fig. 17(a) and (b), respectively. The results are obtained with natural convection cooling. For the integrated inductor case, ferrite cores are fixed between two epoxy resin boards. The transformer and inductance coils are nested. Consequently, ferrite temperatures can be only observed within the dotted area in Fig. 17(a). From Fig. 8, the flux density should be at maximum within this part of the ferrite cores. From Fig. 17, the maximum operating core temperatures are 32 °C and 65 °C, respectively, in an ambient of 22 °C.

From the configurations of the three cases in Table IV and system performance in Figs. 15–17, a pair of PQ 40/40 ferrite cores can be removed from the proposed integration structure with little impact. The reduced volume would be approximately 20 cm^3. The integrated inductor coil does not add significant volume to the system. For the nominal output power, the proposed integration method with a 7.8-mm airgap has higher system efficiency than the other two cases. This mainly results from a lower core flux density. It should be noted that the efficiency improvement between case I and case II/III is limited. However, the volume and operating temperature decreases are substantial.

The experimental results for the system output voltage and dc–dc conversion efficiency given lateral, vertical, and axial misalignment are shown in Figs. 18 and 19. For these misalignment cases, the load resistance is held at 30 Ω. The output voltage and the system efficiency decrease as the coupling coefficient decreases, with nearly the same behavior for misalignment in the x and y directions. The minimum system efficiency is 91.6% for 150 mm lateral or vertical misalignment. For axial misalignment cases, the coupling coefficient retains its highest value, as do the voltage gain and efficiency. The trends follow the simulation results in Fig. 10 and the relation in (9). The voltage gain

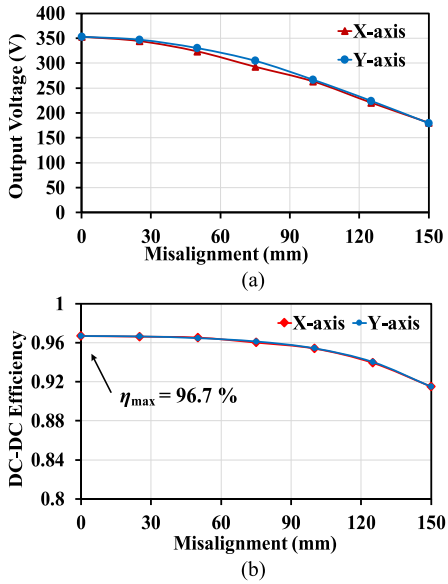

Fig. 18. (a) System output characteristics and (b) dc–dc conversion efficiency for lateral and vertical misalignment.

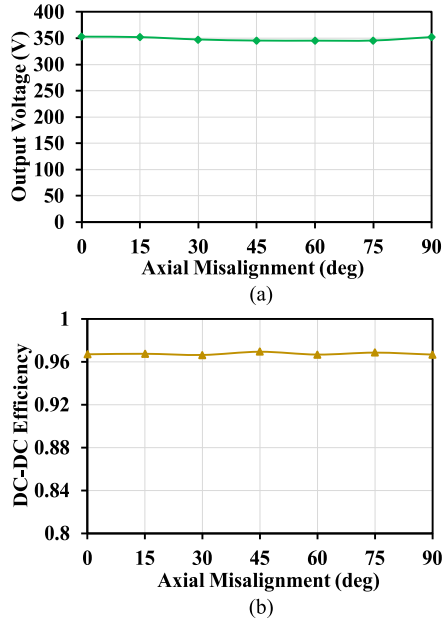

Fig. 19. (a) System output characteristics and (b) dc–dc conversion efficiency for the axial misalignment.

deviations are less than 3% compared with the theoretical results. This shows good agreement.

The experimental waveforms for various load resistances and misalignment cases are shown in Fig. 20. Voltages v_{gs} and v_{ds} are the waveforms measured for one MOSFET in the full-bridge inverter. Here, i_p and i_s represent the primary and secondary resonant currents. The two currents have opposite phases. Their magnitudes decrease as the coupling coefficient decreases and as the load resistance increases. The detailed views of transistor turn-ON are also shown in Fig. 20, demonstrating that the soft-switching conditions are met and that the zero voltage switching

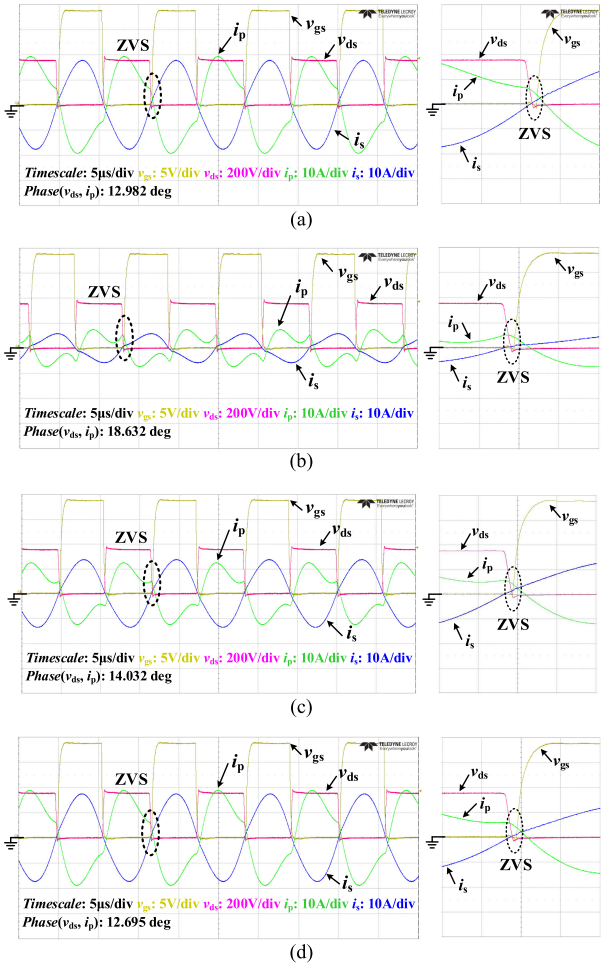

Fig. 20. Experimental waveforms of the IPT system and detailed views on ZVS transitions. (a) At no misalignment (R_L=30 Ω). (b) At no misalignment (R_L=100 Ω). (c) At 100 mm lateral misalignment (R_L=30 Ω). (d) At 45° axial misalignment (R_L=30 Ω).

(ZVS) operation is achieved for various load and misalignment cases.

V. Comparisons Among Magnetic Integration Methods

The magnetic integration methods for IPT systems with planar stacked decoupling structures were described in Section I. Compared with the magnetic integration methods in [18] and [19], the proposed spatially nested integration method in this article inherits the advantages of compact structure, high efficiency, and balanced core magnetic flux density. The reduced volume, improved efficiency, and low peak core temperature have been demonstrated with the experimental results.

The proposed structure has four unique advantages compared with prior methods. First, the airgap width l_g, as shown in Fig. 5, can be adjusted to obtain a precise inductance value. A large airgap has little influence on power coupling characteristics. The simulation results and discussions have been presented in Section III. This contrasts with the prior work [18], [19] in which airgaps among ferrite cores have little impact on integrated inductance values. More FEM simulations on transformer dimensions are required in the prior approach even for minor

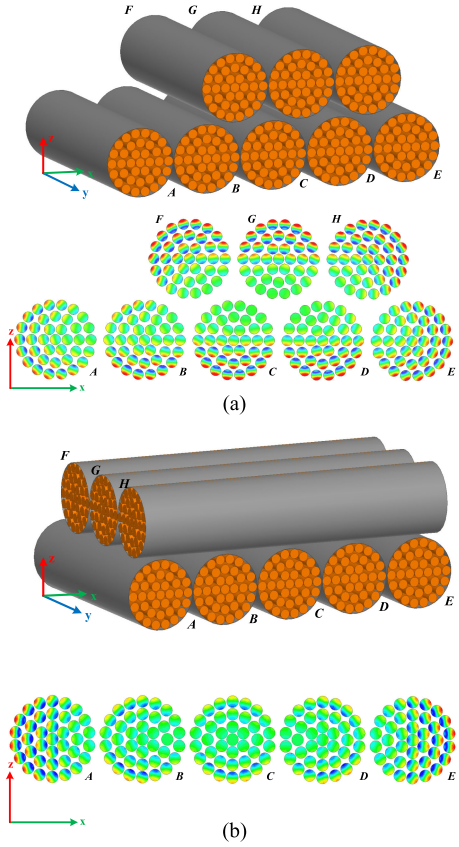

Fig. 21. (a) Parallel coil structures and (b) perpendicular coil structures of two magnetic integration methods with simulation results of the cross-sectional current density distribution.

inductance adjustments, complicating the design process. The proposed method is more effective and more direct for the precise inductance adjustment.

Second, as shown in Fig. 9, the magnetic flux generated by the integrated inductance coil is confined mostly inside the ferrite cores. The magnetic field energy concentrates in the airgap l_g. This decreases the spatial magnetic field leakage.

Third, the nested structure is favorable for decoupling. As shown in Fig. 14, the proposed integration method has no physical position at which a significant cross coupling occurs. The symmetry can be used in the prior work [18], [19] to minimize cross coupling, but this would only be effective for misalignment cases with symmetrical fluxes. For other cases in [18] and [19], cross coupling increases gradually as the coupling reduces. This was shown in [22]. The proposed method is more effective to reduce cross coupling compared with the past work.

Fourth, as shown in Fig. 2, inductance coil P_2 is placed perpendicular to transmitter coil P_1 at overlap points. This structure decreases proximity effects compared with prior structures. The 3-D FEM simulation results for the new structure compared with that in [18] and [19] are shown in Fig. 21 to demonstrate skin and proximity effects. The proximity effects are more obvious in the parallel structure. The proposed structure, at the bottom, shows a much lower impact.

VI. Conclusion

In this article, a spatially nested magnetic structure for IPT systems is proposed to integrate discrete resonant inductors into an IPT transformer. The magnetic flux generated by the unipolar transformer coils and the solenoidal inductance coil is along the radial and tangential directions, respectively. In this case, the coils are orthogonal, so the effects are decoupled for various misalignment cases. An *LCC* series compensation circuit was selected. A 4-kW prototype was implemented and demonstrated the feasibility and validity of the proposed method. The experimental results show that the new compact structure maintains good performance and that there is no physical position at which a significant cross coupling occurs for lateral, vertical, and axial misalignment. The peak efficiency is 96.7% at full power with a 160-mm airgap. The efficiency stays above 91.6% throughout the allowed misalignment range.

Acknowledgment

The work in this article was led by Principal Supervisors H. Ma, D. Xu, and P. Krein.

References

[1] G. A. Covic and J. T. Boys, "Inductive power transfer," *Proc. IEEE*, vol. 101, no. 6, pp. 1276–1289, Jun. 2013.
[2] S. Li and C. C. Mi, "Wireless power transfer for electric vehicle applications," *IEEE J. Emerg. Sel. Topics Power Electron.*, vol. 3, no. 1, pp. 4–17, Mar. 2015.
[3] D. Patil, M. K. McDonough, J. M. Miller, B. Fahimi, and P. T. Balsara, "Wireless power transfer for vehicular applications: Overview and challenges," *IEEE Trans. Transp. Electrific.*, vol. 4, no. 1, pp. 3–37, Mar. 2018.
[4] J. L. Villa, J. Sallan, J. F. S. Osorio, and A. Llombart, "High misalignment tolerant compensation topology for ICPT systems," *IEEE Trans. Ind. Electron.*, vol. 59, no. 2, pp. 945–951, Feb. 2012.
[5] K. Song, Z. Li, J. Jiang, and C. Zhu, "Constant current/voltage charging operation for series–series and series–parallel compensated wireless power transfer systems employing primary-side controller," *IEEE Trans. Power Electron.*, vol. 33, no. 9, pp. 8065–8080, Sep. 2018.
[6] Y. H. Sohn, B. H. Choi, E. S. Lee, G. C. Lim, G.-H. Cho, and C. T. Rim, "General unified analyses of two-capacitor inductive power transfer systems: Equivalence of current-source SS and SP compensations," *IEEE Trans. Power Electron.*, vol. 30, no. 11, pp. 6030–6045, Nov. 2015.
[7] M. Borage, S. Tiwari, and S. Kotaiah, "Analysis and design of an LCL-T resonant converter as a constant-current power supply," *IEEE Trans. Ind. Electron.*, vol. 52, no. 6, pp. 1547–1554, Dec. 2005.
[8] Z. Pantic, S. Bai, and S. M. Lukic, "ZCS LCC-compensated resonant inverter for inductive-power-transfer application," *IEEE Trans. Ind. Electron.*, vol. 58, no. 8, pp. 3500–3510, Aug. 2011.
[9] S. Li, W. Li, J. Deng, T. D. Nguyen, and C. C. Mi, "A double-sided LCC compensation network and its tuning method for wireless power transfer," *IEEE Trans. Veh. Technol.*, vol. 64, no. 6, pp. 2261–2273, Jun. 2015.
[10] L. Zhao, D. J. Thrimawithana, and U. K. Madawala, "Hybrid bidirectional wireless EV charging system tolerant to pad misalignment," *IEEE Trans. Ind. Electron.*, vol. 64, no. 9, pp. 7079–7086, Sep. 2017.
[11] L. Zhao, D. J. Thrimawithana, U. K. Madawala, A. P. Hu, and C. C. Mi, "A misalignment-tolerant series-hybrid wireless EV charging system with integrated magnetics," *IEEE Trans. Power Electron.*, vol. 34, no. 2, pp. 1276–1285, Feb. 2019.
[12] X. Qu, H. Han, S.-C. Wong, C. K. Tse, and W. Chen, "Hybrid IPT topologies with constant current or constant voltage output for battery charging applications," *IEEE Trans. Power Electron.*, vol. 30, no. 11, pp. 6329–6337, Nov. 2015.
[13] R. Mai, Y. Chen, Y. Li, Y. Zhang, G. Cao, and Z. He, "Inductive power transfer for massive electric bicycles charging based on hybrid topology switching with a single inverter," *IEEE Trans. Power Electron.*, vol. 32, no. 8, pp. 5897–5906, Aug. 2017.
[14] W. Li, H. Zhao, S. Li, J. Deng, T. Kan, and C. C. Mi, "Integrated LCC compensation topology for wireless charger in electric and plug-in electric vehicles," *IEEE Trans. Ind. Electron.*, vol. 62, no. 7, pp. 4215–4225, Jul. 2015.
[15] J. Deng, W. Li, T. D. Nguyen, S. Li, and C. C. Mi, "Compact and efficient bipolar coupler for wireless power chargers: Design and analysis," *IEEE Trans. Power Electron.*, vol. 30, no. 11, pp. 6130–6140, Nov. 2015.
[16] F. Lu, H. Zhang, H. Hofmann, W. Su, and C. C. Mi, "A dual-coupled LCC-compensated IPT system with a compact magnetic coupler," *IEEE Trans. Power Electron.*, vol. 33, no. 7, pp. 6391–6402, Jul. 2018.
[17] Z. Yan *et al.*, "Fault-tolerant wireless power transfer system with a dual-coupled LCC-S topology," *IEEE Trans. Veh. Technol.*, vol. 68, no. 12, pp. 11838–11846, Dec. 2019.
[18] T. Kan, T.-D. Nguyen, J. C. White, R. K. Malhan, and C. C. Mi, "A new integration method for an electric vehicle wireless charging system using LCC compensation topology: Analysis and design," *IEEE Trans. Power Electron.*, vol. 32, no. 2, pp. 1638–1650, Feb. 2017.
[19] T. Kan, F. Lu, T.-D. Nguyen, P. P. Mercier, and C. C. Mi, "Integrated coil design for EV wireless charging systems using LCC compensation topology," *IEEE Trans. Power Electron.*, vol. 33, no. 11, pp. 9231–9241, Nov. 2018.
[20] M. Budhia, G. A. Covic, and J. T. Boys, "Design and optimization of circular magnetic structures for lumped inductive power transfer systems," *IEEE Trans. Power Electron.*, vol. 26, no. 11, pp. 3096–3108, Nov. 2011.
[21] H. H. Wu, A. Gilchrist, K. D. Sealy, and D. Bronson, "A high efficiency 5 kW inductive charger for EVs using dual side control," *IEEE Trans. Ind. Inform.*, vol. 8, no. 3, pp. 585–595, Aug. 2012.
[22] A. Zaheer, H. Hao, G. A. Covic, and D. Kacprzak, "Investigation of multiple decoupled coil primary pad topologies in lumped IPT systems for interoperable electric vehicle charging," *IEEE Trans. Power Electron.*, vol. 30, no. 4, pp. 1937–1955, Apr. 2015.
[23] N. Rasekh and M. Mirsalim, "Evaluation study on an integration method for a DDQP using LCC and series compensation topologies for inductive power transfer," *IET Electr. Power Appl.*, vol. 12, no. 9, pp. 1320–1327, Nov. 2018.
[24] Y. Zhang, L. Wang, Y. Guo, and C. Tao, "Null-coupled magnetic integration for EV wireless power transfer system," *IEEE Trans. Transp. Electrific.*, vol. 5, no. 4, pp. 968–976, Dec. 2019.
[25] S. Chen, Y. Chen, N. A. Dung, R. Mai, and Y. Tang, "A compact wireless charger design with decoupled quadruple-D inductor for LCC-series topologies," in *Proc. IEEE Int. Future Energy Electron. Conf.*, Nov. 2019, pp. 1–7.
[26] "Wireless power transfer for light-duty plug-in/electric vehicles and alignment methodology," SAE Standard J2954_201904, 2019. [Online]. Available: http://saemobilus.sae.org/content/J2954_201904/
[27] R. L. Steigerwald, "A comparison of half-bridge resonant converter topologies," *IEEE Trans. Power Electron.*, vol. 3, no. 2, pp. 174–182, Apr. 1988.
[28] E. Laveuve, J.-P. Keradec, and M. Bensoam, "Electrostatic of wound components: Analytical results, simulation and experimental validation of the parasitic capacitance," in *Proc. Conf. Rec. IEEE Ind. Appl. Soc. Annu. Meeting*, Sep./Oct. 1991, pp. 1469–1475.
[29] F. Blache, J.-P. Keradec, and B. Cogitore, "Stray capacitances of two winding transformers: Equivalent circuit, measurements, calculation and lowering," in *Proc. IEEE Ind. Appl. Soc. Annu. Meeting*, Oct. 1994, pp. 1211–1217.
[30] J. Biela and J. W. Kolar, "Using transformer parasitics for resonant converters—A review of the calculation of the stray capacitance of transformers," *IEEE Trans. Ind. Appl.*, vol. 44, no. 1, pp. 223–233, Jan./Feb. 2008.

Zhuhaobo Zhang (Student Member, IEEE) received the B.S. degree in electrical engineering in 2017 from Zhejiang University, Hangzhou, China, where he is currently working toward the Ph.D. degree in electrical engineering.

His main research interests include wireless power transfer, resonant converters, and electric vehicle charging systems.

Shaoting Zheng received the B.S. degree in electrical engineering in 2019 from Zhejiang University, Hangzhou, China, where he is currently working toward the Ph.D. degree in electrical engineering.

His research interests focus on wireless power transfer.

Zirui Yao (Student Member, IEEE) received the B.S. degree in electrical engineering in 2018 from the South China University of Technology, Guangzhou, China, where he is currently working toward the Ph.D. degree in electrical engineering.

His research interests include inductive power transfer and resonant converters.

Dehong Xu (Fellow, IEEE) was born in China, in 1961. He received the B.S., M.S., and Ph.D. degrees from the College of Electrical Engineering, Zhejiang University, Hangzhou, China, in 1983, 1986, and 1989, respectively.

Since 1996, he has been a Full Professor with the College of Electrical Engineering, Zhejiang University. From June 1995 to May 1996, he was a Visiting Scholar with the University of Tokyo, Tokyo, Japan. From June to December 2000, he was a Visiting Professor with the Center for Power Electronics Systems, Virginia Polytechnic Institute and State University, Blacksburg, VA, USA. From February 2006 to April 2006, he was a Visiting Professor with ETH Zurich, Zurich, Switzerland. He has authored or coauthored eight books and more than 270 IEEE journal and conference papers. He holds more than 50 patents. From 2015 to 2017, he was an IEEE PELS Distinguish Lecturer. His current research interests include power electronics topologies and control, and power conversion for renewable energy and energy saving.

Dr. Xu was a recipient of seven IEEE journal and conference paper awards, and the IEEE PELS R. D. Middlebrook Achievement Award in 2016.

Philip T. Krein (Fellow, IEEE) received the B.S. degree in electrical engineering and the B.A. degree in economics and business from Lafayette College, Easton, PA, USA, in 1978, and the M.S. and Ph.D. degrees in electrical engineering from the University of Illinois at Urbana-Champaign, Champaign, IL, USA, in 1980 and 1982, respectively.

He was an Engineer with Tektronix, Inc., Beaverton, OR, USA, and then returned to the University of Illinois at Urbana-Champaign. From 1997 to 1998, he was a Senior Fulbright Scholar with the University of Surrey, Guildford, U.K. From 2003 to 2014, he was a Founder and Director of SolarBridge Technologies, Austin, TX, USA, a developer of long-life integrated inverters for solar energy, and currently a part of Enphase. He holds the Grainger Endowed Chair Emeritus in electric machinery and electromechanics and is the Director of the Grainger Center for Electric Machinery and Electromechanics, University of Illinois at Urbana-Champaign. He is also the Executive Dean of the Zhejiang University–University of Illinois Institute for Engineering, Haining, China. He holds 42 U.S. patents. His current research interests include all aspects of power electronics, machines, drives, electric transportation, and electrical energy, with an emphasis on nonlinear control approaches.

Dr. Krein was a recipient of the IEEE William E. Newell Award in Power Electronics in 2003. He is an Associate Editor for the IEEE *Open Journal of Power Electronics*. He is a Registered Professional Engineer in Illinois and Oregon. He is a past President of the IEEE Power Electronics Society and is also the past Chair of the IEEE Transportation Electrification Community. He was a member of the IEEE Board of Directors, and also the U.S. National Academy of Engineering. He is a fellow of the U.S. National Academy of Inventors.

Hao Ma (Senior Member, IEEE) received the B.S., M.S., and Ph.D. degrees from Zhejiang University, Hangzhou, China, in 1991, 1994, and 1997, respectively, all in electrical engineering.

Since 1997, he has been a Lecturer, an Associate Professor, and a Professor with Zhejiang University. From 2007 to 2008, he was a Delta Visiting Scholar with the North Carolina State University. He is currently the Vice Dean of the Zhejiang University–University of Illinois at Urbana-Champaign Institute, Haining, China. He has authored two books and has authored or coauthored more than 200 technical papers. His current research interests include advanced control in power electronics, wireless power transfer, fault diagnosis of power electronic circuits and systems, and application of power electronics.

Dr. Ma is an Associate Editor for the IEEE JOURNAL OF EMERGING AND SELECTED TOPICS IN POWER ELECTRONICS and the JOURNAL OF POWER ELECTRONICS. He is currently the Director of the Academic Committee of China Power Supply Society. He was the AdCom Member of the IEEE Industrial Electronics Society and the Technical Program Chair of the IEEE ISIE 2012, IEEE PEAC 2014, and IEEE PEAC 2018.